Mathematical Estimation of Particulate Air Pollution Levels by Aerosols Tomography

Or Vernik, Amir Degani, and Barak Fishbain

***Abstract*—Air pollution control and mitigation are important factors in wellbeing and sustainability. To this end, air pollution monitoring has a significant role. Today, air pollution monitoring is mainly done by standardized stations. The spread of those stations is sparse and their cost hinders the option of adding more. Thus, arises the need for cheaper and available means to assess air pollution. In this article, a mathematical method to solve the inverse problem of aerosols tomography is proposed. The suggested method applies filtered back-projection method on a pixel-wise blur estimation. Using the method, particles' concentrations in a 3D space is reconstructed from photos taken from different angles. The proposed method is shown to be very effective for assessing air pollution levels by means of multi angle imaging. Specifically, estimating images' blur as an indication for Particulate Matter (PM) ambient levels. The results of the research point towards strong correlation between image blur and pollution level in the medium and the ability to reconstruct the aerosols distribution in space.**

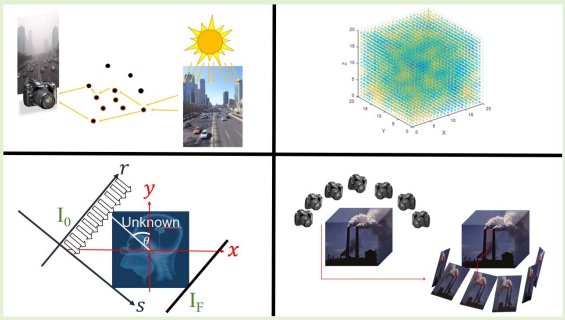

***Index Terms*— Air pollution monitoring, filtered back projection, Monte-Carlo, multi-angle imaging.**

I. Introduction

PARTICULATE Matter (PM) is a mixture of particles suspended in the air that may result from direct emissions or by chemical reaction of other gaseous pollutants (e.g., salts, fossil fuel, nitrates and sulphates). Exposure to PM is known to be one of the predominant factors in morbidity and mortality, causing the premature death of millions of people a year [1]–[3]. Thus, measuring and monitoring PM pollution is an important task the world needs to deal with in order to ensure public health.

Currently, PM monitoring is standardly done by Air Quality Monitoring (AQM) stations that are considered accurate. Examples for AQM use can be found in Latin America [4], China [5] and Israel [6] among other places. Due to their size and cost, the stations are sparsely dispersed, resulting in a low-resolution concentration map. This limitation is typically addressed by interpolation schemes [7]. However, the interpolation is a complicated task as PM concentrations are characterized by high spatial variability and may present different behaviours for different fractions and geographical areas [8].

These drawbacks have led researchers to seek other approaches for air pollution monitoring, either high-resolution devices or less costly and portable monitors, i.e., Micro Sensing Units (MSUs) [6], [9]. These methods can be used for taking measurements, validating new technologies or guidance of interpolating in-situ measurements. MSU-based methods, although answering the price and portability requirements, are not a reliable source for assessing air pollution on their own [9], [10] and an ideal method is yet to be found [1], [6], [9], [11].

Methods for retrieving PM by multi-angle imaging are in use by satellites. Instruments such as Multi-angle Imaging SpectroRadiometer (MISR) and Airborne Multi-angle SpectroPolarimetric Imager (AirMSPI) are currently applied for remote sensing of aerosols [12], [13]. However, these devices have the disadvantage of measuring the full vertical atmospheric column, making their measurements less relevant to the amount of pollution at ground level, that can indicate health hazards [14]. The retrieval of PM concentration from the optical depth measurements is highly dependent on aerosol type, relative humidity (RH), planetary boundary layer height (PBLH), wind speed and direction, and the vertical structure of aerosol distribution [15].

Manuscript received February 25, 2022; accepted March 2, 2022. Date of publication March 15, 2022; date of current version April 29, 2022. This work was supported in part by the Israeli Ministry of Science and Technology under Grant 3-15628 and in part by the Israeli Ministry of Environmental Protection. The associate editor coordinating the review of this article and approving it for publication was Prof. Chao Tan. *(Corresponding author: Or Vernik.)*

Or Vernik is with the Department of Applied Mathematics, Faculty of Mathematics, Technion–Israel Institute of Technology, Haifa 3200003, Israel (e-mail: orver@campus.technion.ac.il).

Amir Degani and Barak Fishbain are with the Department of Environmental, Water and Agriculture Engineering, Faculty of Civil and Environmental Engineering, Technion–Israel Institute of Technology, Haifa 3200003, Israel (e-mail: adegani@cv.technion.ac.il; fishbain@cv.technion.ac.il).

Digital Object Identifier 10.1109/JSEN.2022.3158890

In this work, we focus on *visual* means for assessing PM levels in the atmosphere. An image processing technique for deriving quantitative measurement of visibility, using Red-Green-Blue (RGB) standard camera network, was suggested by Graves and Newsam [16]. The method evaluates the extinction coefficient β, a measure that quantifies local radiance attenuation and is used as a standard for measuring atmospheric visibility. To this end, the atmospheric transmission t (the ability of radiation to pass through the atmosphere) is derived from standard photos, based on image analysis techniques such as local image contrast and dark channel prior. For l, the length of the visual pathway, assuming homogeneous atmosphere throughout the scene, the transmittance has a simplified closed form, inverse relationship, with the extinction coefficient:

$$t(x) = e^{-\beta \times l}. \tag{1}$$

It is important to note that the assertion of homogeneous atmosphere often does not hold in reality [17]. Thus, equation (1) is an approximation of the relationship, neglecting other components effects and physical phenomena such as hygroscopic growth of aerosols.

This research aims at improving this notion, by looking at a 3D volume with changing concentrations at each voxel (as opposed to the homogeneous atmosphere assumption made by Graves and Newsam), attaining a quantitative measurement for PM concentration at each voxel (volume element). The underlying assumption here is that due to the particles' optical properties of scattering, different concentrations of particles will cause the light field to scatter differently [14]. The higher the concentration of scatterers, the more refractions the light will go through. Refracted light impairs human visibility and expression for this phenomenon manifests itself in standard photos [16]. Particles suspended in the air cause a level of blurriness in the acquired photo. Having this relationship between blurriness and amount of scatterers in the air leads us to the approach of estimating the particles' concentration by measuring image blurriness.

The blur of an image is positively correlated with the integral of the attenuation (extinction) coefficient over the Line Of Sight (LOS) to the object. Thus, by measuring the blurriness of one image we cannot infer the concentration at each voxel. The initial intensity of the light's direct transmission (I_0) is attenuated by the scattering (here we assume that the absorption by particulate matter is mostly negligible) and I, the measured radiation intensity is computed by:

$$I = I_0 e^{-\int_{LOS} \beta(l) dl}. \tag{2}$$

Our objective then is to find β, which is strongly related to the PM concentration. Let Ω be the volume in which we would like to measure PM concentrations; let $\omega = (x, y, z) \in \Omega$ be a specific location in space; and $n(\omega)$ denotes the PM concentration at position ω. Having σ as the extinction cross section, β is the result of multiplication of the two:

$$\beta(\omega) = \sigma \cdot n(\omega). \tag{3}$$

The extinction cross section, σ, depends upon the light's wavelength and the particle's shape and size. For our purposes it is assumed spherical shaped particles of a constant size. Assuming we know the values of the extinction coefficient integral for a large number of angles (having a correlation with the blurriness measure), the inverse problem is mathematically solvable by the Radon transform [18].

Radon transform is widely used in Computational Tomography (CT) applications, allowing us to reconstruct the object being scanned from its measured projections. The classically used form of the Radon transform and that we are going to describe, is the 2D Radon, for each reconstruction, z-coordinate will be considered constant. A projection is the integral over the extinction coefficient which, using equation (2), equals to:

$$p(x, y) = \int \underbrace{\beta(x, y)}_{\substack{\text{our} \\ \text{objective}}} dy = \underbrace{-\ln\left(\frac{I(y)}{I_0}\right)}_{\text{assumed known}}. \tag{4}$$

The projections are assumed to be known in regular CT scans as we have a controlled radiation source, with known initial intensity I_0, and the final intensity, I, is measured by the scanner when exiting the body.

The most effective way for reconstructing β from the projections is by using Filtered Back Projections (FBP) that is equivalent to the Inverse Radon Transform (IRT) but less computationally costly. Let θ be the angle in which the rays are sent, in relation to the X-axis (rays are sent parallel for each image), and let R be the displacement of projection on the axis perpendicular to θ (the radiation detector location along the axis). The Radon Transform is simply a transformation of the projections from the image X-Y plane to the plane of R-θ lines (also called the Sinogram image).

The Radon transform represents the data as it is obtained in scanning an object through lines in different angles of the body. The reconstruction is done using FBP on the Sinograms received. The projections are convolved ('$*$' operator) with High Pass Filter (HPF), $q(r)$, called ramp filter, before being back projected, arriving at:

$$C(x, y) = \int_0^{\pi} p(r, \theta) * q(r) d\theta. \tag{5}$$

The filter is convolved with the projections in order to prevent blurring effects in the reconstructed image. Although ideally using ramp filter results in an exact reconstruction, when projections are impaired with noise, HPF has the undesirable effect of magnifying it. A more commonly used and suitable filter is the Ram-Lak filter [19].

Relying on the above principals, a new mathematical method to solve the inverse problem of aerosols tomography is proposed. The Radon transform is used in specific conditions where the radiation source is controlled. Rays are sent at a certain angle with known initial intensity and the intensity on the other side of the medium (usually a body) can be measured. Thus, the values of the projections for each angle can be easily computed. We suggest to use a pixel-wise blur measure to replace the projections value. Doing so, there is no need in knowing the initial rays' intensity or measure the exact final intensity. We use the Monte-Carlo method as the image formation model and reconstruct the original concentrations

using filtered back projection method with image blur values as the integral over the concentrations.

It is known that pixel blur estimation will only be valuable on image edges, whereas inside homogeneous areas blur could not be detected. Our expectations are to have good reconstructions around contamination edges when a strong homogeneous pollution cloud is imaged, or, next to scenery edges when there is a less visible contamination. In practice, the PM concentration has high spatial variability and is not usually homogeneous. For this type of pollution, we expect good reconstruction.

We have tested the reconstruction scheme with different scenarios and found it to be useful for generating 3D dense map of the area of contamination, giving highly accurate value for the particle concentration.

II. Methodology

Our experiment consists of two parts. The first is deriving images of the scene, subjected to air pollution blur. The second, reconstructing the concentrations based only on the first stage results, i.e., the images. The second part contains our conjuncture that reconstruction is possible solely based on images' blur, and the first is the platform for testing it.

A. Constructing the Images

To examine the potential of the suggested method, we designed a simulation of the image acquisition process of the light field in a 3D volume, using the Monte-Carlo method [20]. This extends the work of Vernik and Fishbain [21], in which, the blur effect was demonstrated on a 2D plane.

For the mathematical description of the problem, let us recapitulate the notation above. We define a 3D rectangular volume domain $\Omega \subset R^3$, with parameters $\{a, b, c\}$ defining the extent of the volume, as:

$$\Omega = \{(x, y, z) : 0 < x < a, 0 < y < b, 0 < z < c, a, b, c \in R\}. \tag{6}$$

At each voxel $\omega = (x, y, z) \in \Omega$, the extinction coefficient $\beta(\omega)$, is defined, depending on the concentration map we wish to simulate.

We relate to the physical behaviour of light propagating through a volume containing PM in different concentrations as a random process [22]. The light, taken in its particulate sense of photons, passes a medium, which has spatially variable optical depth (a measure of the light ability to propagate through the medium) denoted by τ. At each stage, τ is sampled from the optical depth Cumulative Density Function (CDF):

$$F(\tau) = \int_0^{\tau} e^{-\tau'} d\tau' = 1 - e^{-\tau}. \tag{7}$$

Using the Monte-Carlo method, we get a random optical depth sampled from its CDF. For this, we use the uniform distribution (U[0,1]) CDF for sampling a random number u, and derive τ by:

$$\tau = F^{-1}(u). \tag{8}$$

By using the random τ we sampled, we can determine l, the distance the ray propagates until the next diffraction. Let σ be the extinction cross section, and n, the PM concentration at each voxel ω. The distance, l, is computed using numerical integration over β based on the following relationship:

$$\tau = \int_0^l \beta(\omega) dl = \int_0^l \sigma \cdot n(\omega) dl. \tag{9}$$

Once l is found, the scattering angle after the collision has to be determined. The angle is computed in a similar fashion, assuming randomness in the process and relying on Mie scattering theorem under the assumption of spherical particles [23]. The Mie-Lorenz theorem provides a physical solution for the scattering of an electromagnetic wave by spherical uniform particles about the size of the light wavelength. Computing the scatter angle using the theorem involves computing an infinite series and is considered a complicated numerical task. Often, the solution for the scattering angle is approximated. In this study, we chose the Henyey-Greenshtein phase function (HGPF) approximation due to its simplicity, involving only one parameter. Defining $\mu = \cos\theta$ and g as the asymmetry parameter indicating type of scattering (ranges from backscattering to forward), HGPF provides the probability of a photon to be scattered at a certain angle θ:

$$P(\mu) = \frac{1}{2} \frac{1 - g^2}{(1 + g^2 - 2g\mu)^{\frac{3}{2}}}. \tag{10}$$

There are several methods for deriving the Mie-equivalent aerosol asymmetry parameter (g) each using a variety of parameters such as particles' size, and RH, among others [24]–[28]. The analysis here observes a finite volume element with light emitted from a single angle at a time. In the analysis done here, the asymmetry parameter, g, was chosen to be close to 1 ($g = 0.99$), corresponding to limited angle change as a result of a collision. In order to find the angle cumulative density function we will integrate over the phase probability function as follows:

$$\begin{aligned} F(\mu) &= \int_{-1}^{\mu} \frac{1}{2} \frac{1 - g^2}{(1 + g^2 - 2g\mu)^{\frac{3}{2}}} dg \\ &= \frac{1 - g^2}{2g} \{(1 + g^2 - 2g\mu)^{-\frac{1}{2}} - (1 + g)^{-1}\}. \end{aligned} \tag{11}$$

Using Monte-Carlo simulation, we will sample a random angle from the HGPF CDF on the intersection plane [22]. At the perpendicular plane, the angle, called the zenith angle, has uniform distribution in the range [0,2π), so it is selected randomly. The found angles, will give us the new direction of the ray's propagation. Each collision will also cause an attenuation in the radiation intensity by a factor of $\bar{\gamma}$, that is the Single Scattering Albedo (SSA), according to aerosols properties, following [29], we used $\bar{\gamma} = 0.9$.

We repeat this process of finding new distance to the next collision, new direction and the intensity at each stage, until the ray exits our defined volume. The described process is done for each ray in the packet of rays entering from each radiated voxel. The image acquisition process is done by summing the values of the exiting rays' intensities for each pixel at the

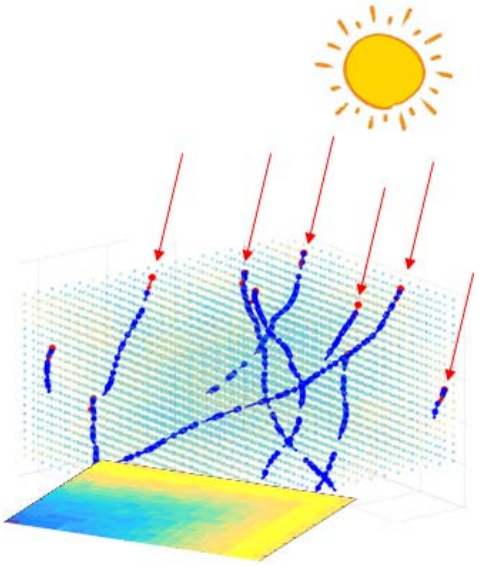

Fig. 1. Sun rays hit the medium and scattered until exiting the grid boundaries. Image is received on the bottom plane as a result of rays intersecting the plane.

desired image plane. visualization of the simulation shown in Figure 1. In the image, our 3D volume is depicted, where the different concentrations at each voxel are marked by colour. The red arrows are the sun rays entering the volume and the blue lines are the paths the radiation goes through in the volume. Finally, we can see the image created on the bottom plane, that is the summation of each pixel entering rays' intensities.

B. Air Pollution Field Reconstruction

First, we wanted to strengthen the conjecture of the correlation between level of pollution in the volume and the received image blurriness. The blurriness of the image is determined by the Blur Metric (BM) suggested by Crete-Roffet *et al.* [30]. The blur metric estimation of the image blurriness is based upon the notion that once an image is blurred, blurring it again will result in smaller differences than blurring a sharp image. Here, this principle is applied on the pixel level. Let $p = (i, j)$ be a pixel in the received image, where for each pixel, p, its blurriness is estimated by its 5×5 neighbourhood.

According to the method we take the image, denoted M_0 (the original image), pass it through a low-pass filter (the averaging filter) and receive a blurred image output (M_1). The averaging filter is then applied on M_1, thus receiving a blurrier result (M_2). Finally, the differences between the original, M_0, and M_1 are compared with the differences between M_1 and M_2. The higher the differences are, the sharper the original image is. The method yields a value between zero and one indicating the effective blurriness of the pixel, relying on its neighbouring pixels.

For testing the correlation, a binary image of 'Lena' [31] is used as our imaged object. Rays are emitted from the image, propagate through the volume and caught by the camera lens. The results are indeed a blurred image of the original Lena (Figure 2). Repeating the same initial conditions only

Fig. 2. From left to right. (left) Lena's original B&W image. (middle) The received image with uniform PM concentration in the volume. (right) The received image with larger PM concentration in the volume (x2).

with growing levels of PM concentrations and measuring the blurriness of the image using our blur metric, gives us a strong correlation between the effective image blur and the level of pollution.

To examine the blur measure ability to reconstruct the PM concentrations, as a replacement for knowing the projections, a simulation is held. In the simulation, a staring camera at a certain angle θ, relates only to the light that enters the volume, i.e., we neglect light coming from other directions. To get accurate results our system takes 180 photos of the medium in 180 evenly spaced degrees at the range $[0, 179]$. This is illustrated in Figure 3. The volume, through which light propagates, contains a box with constant pollution value. Figure 3.a depicts the initial angle of the radiating plane $theta = 0$deg. At this angle the camera is located below the volume looking up. Figures b and c are the same setup under rotation of $\theta = 45°$ and $\theta = 150°$. A reduction of the number of cameras is addressed in the conclusions section. The received photos, in the Monte-Carlo simulation, (each received from a different angle) are used to estimate the level of pollution by applying the blur metric as previously described.

The selected reconstruction method is the filtered back projection. The reconstruction is actually done for slices (X-Z planes) of the volume. For each slice we create the Sinogram of the slice. The Sinogram image consists of the projections of the slice for all angles, where instead of projections, the blur metric value is used. We then reconstruct each slice by preforming FBP on the Sinograms.

III. Results

The experiment was done for many different concentration patterns. First, patterns that have a defined shape were examined, so it would be clear to see the reconstruction results. For example, high uniform concentration in the volume centre and a dumbbell shape concentration map. These are illustrated in Figure 4.a and Figure 4.b, which present the sphere in the center of the volume and the dumbbell respectively.

We simulated with the Monte-Carlo method the rays entering the volume at specific points and angles and diffracting by the particles. The simulation is done for all 180 angles in our range (see Figure 3). For each voxel in the radiation plane we simulate a beam that hits the voxel and propagates through the volume until exiting from the grid boundaries. The process is depicted in Figure 5. Figure 5.a presents a light beam entering the volume at an angle of $\theta = 125°$. Figure b is a zoom into a voxel, where the light is being diflected as a result of

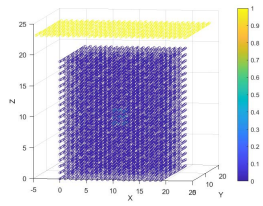

(a) The radiation plane for $\theta = 0\,\text{deg}$

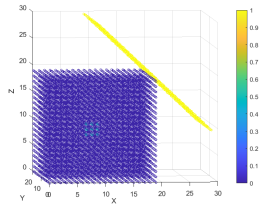

(b) The radiation plane for $\theta = 45\,\text{deg}$

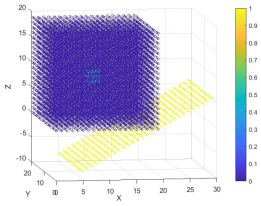

(c) The radiation plane for $\theta = 150\,\text{deg}$

Fig. 3. Radiation planes for three different angles. When the camera is staring at the volume at angle θ, the rays we relate to in the simulation are emitted from the yellow plane.

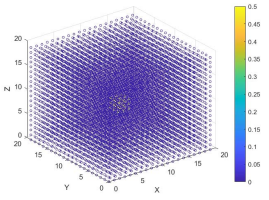

(a) Initial concentration of 0.5 $[m^{-3}]$ in the volume center.

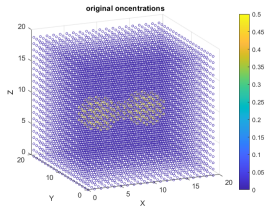

(b) Dumbbell shaped uniform concentration.

Fig. 4. Initial concentrations.

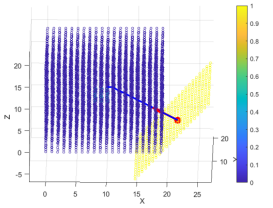

(a) Ray entering at $angle = 125\,\text{deg}$ and scattered by the centred concentration

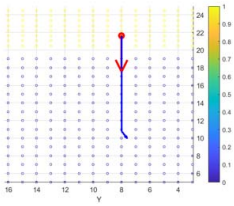

(b) Same ray looking from above, new angle is determined by Monte-Carlo

Fig. 5. Ray's trace in the volume.

Fig. 6. Sinogram of the volume middle layer - centred concentration.

Fig. 7. Sinogram of the volume middle layer using the blur metric - centred concentration.

Fig. 8. Sinogram of the volume middle layer - dumbbell concentration.

Fig. 9. Sinogram of the volume middle layer using the blur metric - dumbbell concentration.

a collision of the light beam with a particle. The image received on the other end of the volume consists of the rays that were scattered within the image plane.

We have performed reconstruction using FBP on images received based on pixels intensity values (the original method, for comparison) and based on blur metric values (our suggested method).

The Sinograms for the middle layer (volume's center X-Z slice) reconstruction, are shown in Figures 6-9. Figures 6 and 7 present the sinograms for the sphere concentration in the volume's center (see Figure 4.a) when taking the image intensity levels and the blur metric respectively. Figures 8 and 9 present the same mid-layer sinograms for the intensity levels and blur metric respectively for the dumbbell shaped pollution (see Figure 4.b).

The sinograms are the projections on *R*-θ plane. For each angle θ (the horizontal axis), we see the projections for all the R's, the locations in the slice, for that angle. As expected, the blur metric Sinogram is approximately an edge image of the original Sinogram. The results of the centered sphere are shown in figure 10, where the lefthand side (a) is the reconstruction using images' intensity levels and the righthand side is the reconstruction of the pollution field through the blur metric values. Similarly, Figure 11 presents the results of the dumbbell shaped pollution, for the intensity levels (Figure 11.a and the blur metric, Figure b. As evident from the results, the projection reconstruction is much more accurate. Albeit, the blur metric also gives good estimation for the concentrations at the edges although poor results in the homogeneous area. This experiment was done for several levels of concentrations, for different shapes and types of concentrations. The more variant the concentration is, the more accurate the blur metric reconstruction is, in some cases, such as randomized concentration (shown next), even more accurate than the original method.

The aforementioned experiment ran with the Lenna image. While presenting a wide range of spatial frequencies [32], the Lenna image is less representative of a scenery figure,

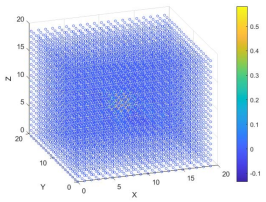

(a) The 3D reconstruction result.

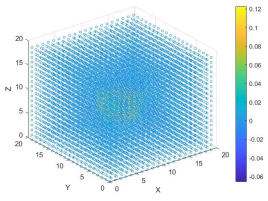

(b) The 3D reconstruction result using BM.

Fig. 10. Centered concentration.

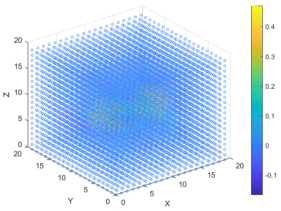

(a) The 3D reconstruction result.

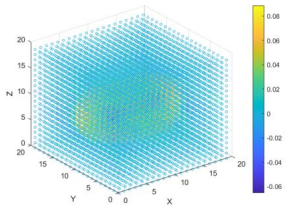

(b) The 3D reconstruction result using BM.

Fig. 11. Dumbbell concentration.

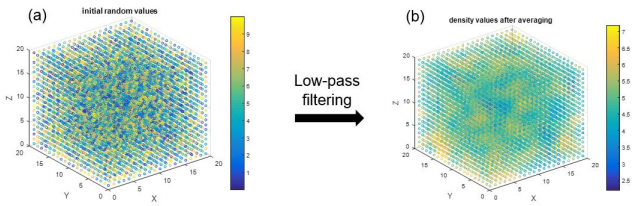

Fig. 12. Initial uniform random values in the range [0,10] (a) and the smoother version with smaller spatial gradients in concentration (b).

Fig. 13. The images scenery.

which is more likely to be obtained in applications which aims at inferring ambient PM levels. To simulate the system with more representative image, the experiment was repeated with a scenery image. To this end, we used a black and white panorama image of New-York city. The panorama image filters the incoming rays, as if the rays are coming from this scenery.

Photos were acquired in the same manner as previously described. Reconstruction using Radon is performed after subtracting the images received with the images received with zero concentration at the volume, in order to remove scenery. In blur reconstruction, this action is not needed, scenery is what enables us to better reconstruct, relying on its edges. The results are very good with error two orders of magnitude lower than concentrations level, with a maximum error of 0.007. To show the results visually clearer, we present the average of the volume on the Z-axis.

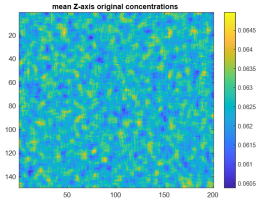

(a) The original concentrations averaged on the Z-axis

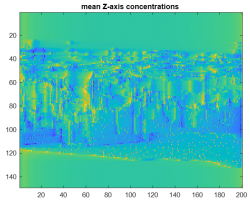

(b) The reconstruction using projections, averaged on the Z-axis

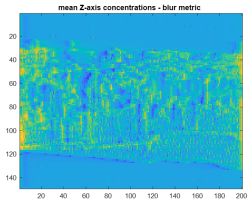

(c) The reconstruction using BM, averaged on the Z-axis

Fig. 14. Results for random concentration.

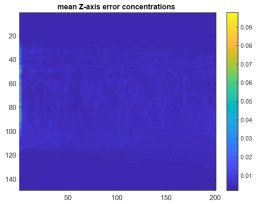

(a) The reconstruction error using projections averaged on the Z-axis

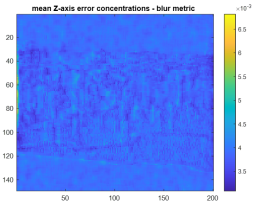

(b) The reconstruction error using projections averaged on the Z-axis

Fig. 15. Reconstructions errors.

TABLE I
PM ESTIMATION RESULTS FOR THE SPHERE, DUMBBELL AND NEW-YORK INPUT IMAGES. THE ERROR IS PRESENTED FOR THE RECONSTRUCTION USING EITHER IMAGE INTENSITY LEVELS AND THE BLUR MATIC

	MSE - Intensity Levels	MSE - Blur-Metric
Sphere	0.0036	0.005
Dumbell	0.0348	0.053
New-York	0.0182	0.004

The random concentration is created by drawing random values at each voxel, as illustrated in Figure 12a, and smoothing the result with a 3D box filter. That, in order to create a more realistic distribution (Figure 12b). Results are shown in Figure 14 and errors shown in Figure 15. Notice the scale in relation to the original concentrations, the error is two scales lower.

IV. CONCLUSION AND FUTURE WORK

Overall we presented here a full back projection based reconstruction scheme used for finding the original concentrations in space, having only the images as input. The mean squared estimation errors of PM levels estimation in each voxel is presented in Table I. The results are presented for

the sphere and dumbbell pollution patterns, as well as for the New-York city. The PM estimation errors are presented for all the scenes, using either image intensity levels or the blur metric.

The results indicate that not only there is a correlation between image blur and pollution level in the medium, the blur metric can be used as a good estimation for the PM concentrations. Another important conclusion is that the method actually finds the concentrations contour. The method is most effective when concentrations are spread in space and not mostly homogeneous.

The advantages of using the blur metric over the projections are numerous. We benefit discarding the need to know the initial rays' intensity or the ratio between measured rays' intensity to the initial ones. In our suggested method, reconstruction is done solely based on images. Other blur metrics will be also used for comparison in future work [33], [34].

The system discussed here is integral based. Hence, it tends to be stable and presents small perturbation at the system's output as a result of small perturbation at its inputs. Therefore, we expect this theoretical exercise to show similar results in real-life applications. Also, assumptions that were made in order to test our hypothesis can be removed one by one and the results should still hold. Such assumption is that rays are coming from one direction, without light coming from the sides. Because blur is an integrative linear measurement that relates to how blurry the pixel is relative to its corresponding front, we believe that the results will be close to the ones we got here with the underlying assumption. If so, next stage will be a field campaign to test this scenario.

Finding the end cases, for which this method works best and does not work well, are also important as we continue our work. The ways in which this research can develop are endless, as we can work on improving the method (better modelling of the light field, ground reflections, time dependency and more.), testing its results for variety of scenarios (simulative or experimental).

Currently, we apply the method using many angles of shot. We are aware of that being a complicated task and we stress the fact that this was essential for testing the sole feasibility of the idea. Now, with this concept proven, we aim at lowering the number of angles needed for the reconstruction as was shown in [35] and [36]. A good challenge will also be testing what will be the turning point in terms of accuracy where lowering the number of cameras downgrades the method greatly.

Due to the method being useful only on edges, it is possible to decide a complementary method. The method could fill in the missing concentrations, when realizing that concentrations are largely homogeneous. This can be done by image processing means and will be explored in the future.

REFERENCES

[1] N. Castell *et al.*, "Can commercial low-cost sensor platforms contribute to air quality monitoring and exposure estimates?" *Environ. Int.*, vol. 99, pp. 293–302, Feb. 2017. [Online]. Available: http://www.sciencedirect.com/science/article/pii/S0160412016309989

[2] X. Yang *et al.*, "Health risk and disease burden attributable to long-term global fine-mode particles," *Chemosphere*, vol. 287, Jan. 2022, Art. no. 132435.

[3] J. S. Apte, J. D. Marshall, A. J. Cohen, and M. Brauer, "Addressing global mortality from ambient $PM_{2.5}$," *Environ. Sci. Technol.*, vol. 49, no. 13, pp. 8057–8066, Jul. 2015.

[4] J. F. Franco, L. Gidhagen, R. Morales, and E. Behrentz, "Towards a better understanding of urban air quality management capabilities in Latin America," *Environ. Sci. Policy*, vol. 102, pp. 43–53, Dec. 2019.

[5] H. Fan, C. Zhao, and Y. Yang, "A comprehensive analysis of the spatio-temporal variation of urban air pollution in China during 2014–2018," *Atmos. Environ.*, vol. 220, Jan. 2020, Art. no. 117066.

[6] S. Moltchanov, I. Levy, Y. Etzion, U. Lerner, D. M. Broday, and B. Fishbain, "On the feasibility of measuring urban air pollution by wireless distributed sensor networks," *Sci. Total Environ.*, vol. 502, pp. 537–547, Jan. 2015, doi: 10.1016/j.scitotenv.2014.09.059.

[7] Q. Tan *et al.*, "Increasing impacts of the relative contributions of regional transport on air pollution in Beijing: Observational evidence," *Environ. Pollut.*, vol. 292, Jan. 2022, Art. no. 118407. [Online]. Available: https://www.sciencedirect.com/science/article/pii/S0269749121019898

[8] J. P. Pinto, A. S. Lefohn, and D. S. Shadwick, "Spatial variability of $PM_{2.5}$ in urban areas in the united states," *J. Air Waste Manage. Assoc.*, vol. 54, no. 4, pp. 440–449, Feb. 2012.

[9] B. Fishbain *et al.*, "An evaluation tool kit of air quality micro-sensing units," *Sci. Total Environ.*, vol. 575, pp. 639–648, Jan. 2017. [Online]. Available: http://www.sciencedirect.com/science/article/pii/S0048969716319799

[10] F. Kizel *et al.*, "Node-to-node field calibration of wireless distributed air pollution sensor network," *Environ. Pollut.*, vol. 233, pp. 900–909, Feb. 2018, doi: 10.1016/j.envpol.2017.09.042.

[11] U. Lerner, O. Hirshfeld, and B. Fishbain, "Optimal deployment of a heterogeneous environmental sensor network," *J. Environ. Inform.*, vol. 2016, no. 1, pp. 99–107, Aug. 2016.

[12] D. J. Diner *et al.*, "Multi-angle Imaging SpectroRadiometer (MISR) instrument description and experiment overview," *IEEE Trans. Geosci. Remote Sens.*, vol. 36, no. 4, pp. 1072–1087, Jul. 1998.

[13] D. J. Diner *et al.*, "The airborne multiangle SpectroPolarimetric imager (AirMSPI): A new tool for aerosol and cloud remote sensing," *Atmos. Meas. Techn.*, vol. 6, no. 8, pp. 2007–2025, Aug. 2013.

[14] Y. Etzion, D. Broday, and B. Fishbain, "Analysis of image color and effective bandwidth as a tool for assessing air pollution at urban spatiotemporal scale," *Proc. SPIE Int. Soc. Opt. Eng.*, vol. 8657, Feb. 2013, Art. no. 86570U.

[15] C. Zheng *et al.*, "Analysis of influential factors for the relationship between $PM_{2.5}$ and AOD in Beijing," *Atmos. Chem. Phys.*, vol. 17, no. 21, pp. 13473–13489, 2017. [Online]. Available: https://acp.copernicus.org/articles/17/13473/2017/

[16] N. Graves and S. Newsam, "Using visibility cameras to estimate atmospheric light extinction," in *Proc. IEEE Workshop Appl. Comput. Vis. (WACV)*, Jan. 2011, pp. 577–584.

[17] C. Zhao *et al.*, "Estimating the contribution of local primary emissions to particulate pollution using high-density station observations," *J. Geophys. Res., Atmos.*, vol. 124, no. 3, pp. 1648–1661, Feb. 2019.

[18] L. P. Yaroslavsky, *Digital Holography and Digital Image Processing: Principles, Methods, Algorithms*. Boston, MA, USA: Kluwer, 2004.

[19] J. Bernal and J. Sanchez, "Use of filtered back-projection methods to improve ct image reconstruction," Tech. Rep., Sep. 2009. [Online]. Available: https://www.researchgate.net/publication/265811375_Use_of_Filtered_Back-projection_Methods_to_Improve_CT_Image_Reconstruction/citations

[20] R. Y. Rubinstein and D. P. Kroese, *Simulation Monte Carlo Method*, 3rd ed. Hoboken, NJ, USA: Wiley, 2016.

[21] O. Vernik and B. Fishbain, "Mathematical estimation of particulate air pollution levels by multi-angle imaging," in *Environmental Software Systems Data Science in Action*, I. N. Athanasiadis, S. P. Frysinger, G. Schimak, and W. J. Knibbe, Eds. Cham, Switzerland: Springer, 2020, pp. 249–257.

[22] A. Levis, Y. Schechner, A. Aides, and A. Davis, "Airborne three-dimensional cloud tomography," in *Proc. Int. Conf. Comput. Vis.*, Dec. 2015, pp. 3379–3387.

[23] J. E. Hansen and L. D. Travis, "Light scattering in planetary atmospheres," *Space Sci. Rev.*, vol. 16, no. 4, pp. 527–610, 1974.

[24] A. A. Kokhanovsky, *Satellite Aerosol Remote Sensing Over Land*, 1st ed. Berlin, Germany: Springer, 2009.

[25] E. Andrews *et al.*, "Comparison of methods for deriving aerosol asymmetry parameter," *J. Geophys. Res.*, vol. 111, no. D5, pp. 5–9, 2006. [Online]. Available: https://onlinelibrary.wiley.com/doi/full/10.1029/2004JD005734
[26] O. Boucher, "On aerosol direct shortwave forcing and the henyey–greenstein phase function," *J. Atmos. Sci.*, vol. 55, no. 1, pp. 128–134, Jan. 1998.
[27] V. I. Haltrin, "Two-term Henyey-Greenstein light scattering phase function for seawater," in *Proc. Int. Geosci. Remote Sens. Symp. (IGARSS)*, vol. 2, 1999, pp. 1423–1425. [Online]. Available: https://www.osapublishing.org/abstract.cfm?uri=ao-41-6-1022
[28] K. Kamiuto, "Study of the henyey-greenstein approximation to scattering phase functions," *J. Quant. Spectrosc. Radiat. Transf.*, vol. 37, no. 4, pp. 411–413, Apr. 1987.
[29] R. C. Levy, *Satellite Aerosol Remote Sensing Over Land*. Berlin, Germany: Springer, 2009, pp. 19–69.
[30] F. Crété-Roffet, T. Dolmière, P. Ladret, and M. Nicolas, "The blur effect: Perception and estimation with a new no-reference perceptual blur metric," *Proc. SPIE Hum. Vis. Electron. Imag.*, vol. 12, Mar. 2007, Art. no. 64920I.
[31] D. C. Munson, "A note on Lena," *IEEE Trans. Image Process.*, vol. 5, no. 1, p. 3, Jan. 1996.
[32] L. Roberts, "Picture coding using pseudo-random noise," *IRE Trans. Inf. Theory*, vol. 8, no. 2, pp. 145–154, Feb. 1962.
[33] F. Kerouh and A. Serir, "A, no., reference perceptual blur quality metric in the DCT domain," in *Proc. 3rd Int. Conf. Control, Eng. Inf. Technol. (CEIT)*, May 2015, pp. 1–6.
[34] Z. Li, Y. Liu, J. Xu, and H. Du, "A no-reference perceptual blur metric based on the blur ratio of detected edges," in *Proc. 5th Int. Conf. Broadband Netw. Multimedia Technol.*, 2013, pp. 1–5.
[35] S. Moshenberg, U. Lerner, and B. Fishbain, "Spectral methods for imputation of missing air quality data," *Environ. Syst. Res.*, vol. 4, no. 1, pp. 1–13, Dec. 2015.
[36] L. Yaroslavsky, G. Shabat, B. Salomon, I. Ideses, and B. Fishbain, "Nonuniform sampling, image recovery from sparse data and the discrete sampling theorem," *J. Opt. Soc. Amer. A, Opt. Image Sci.*, vol. 26, pp. 566–575, Apr. 2009.

Or Vernik received the B.Sc. degree in electrical engineering and the M.Sc. degree in applied mathematics from the Technion-Israel Institute of Technology in 2017 and in 2021, respectively. Her research focused on air pollution estimation by visual means.

Amir Degani received the B.Sc. *(summa cum laude)* degree in mechanical engineering from the Technion–Israel Institute of Technology, Haifa, Israel, in 2002, and the M.S. and Ph.D. degrees in robotics from Carnegie Mellon University, Pittsburgh, PA, USA, in 2006 and 2010, respectively.

From 2011 to 2019, he was an Assistant Professor of Civil and Environmental Engineering at the Technion–Israel Institute of Technology, where he has been an Associate Professor since 2019. He is the Director of the Civil, Environmental and Agricultural Robotics (CEAR) Laboratory researching robotic legged locomotion and autonomous systems in civil and agriculture applications. He has six patents in the robotics field. His research interests include mechanism analysis, synthesis, control and motion planning and design with emphasis on minimalistic concepts and the study of nonlinear dynamic hybrid systems.

Prof. Degani was a recipient of the Best Paper Award at the IEEE BioRob Conference in 2006, the Best Video Award at the IEEE ICRA Conference in 2010, and the JTCF Novel Technology Paper Award at IEEE IROS 2015. He is currently an Associate Editor of the IEEE ROBOTICS AND AUTOMATION LETTERS (RA-L), the IEEE TRANSACTIONS ON ROBOTICS (T-RO), the IEEE International Conference on Robotics and Automation (ICRA) and the IEEE Intelligent Robots and Systems (IROS) Conferences.

Barak Fishbain received the Ph.D. degree from the Department of Industrial Engineering and Operations Research (IEOR), University of California at Berkeley. He was an Associate Director of the Integrated Media Systems Center (IMSC), Viterbi School of Engineering, University of Southern California (USC). He is an Associate Professor with the Environmental, Water and Agricultural Engineering Division, Faculty of Civil and Environmental Engineering, Technion–Israel Institute of Technology, Haifa, Israel. His research focuses on Enviromatics—a new research field that aims at devising AI and machine learning methods and mathematical models for better understanding built and natural complex environments. The goal is to harness new machine learning and mathematical models with engineering principles, computing, and networked sensing data analytics for enhancing the efficiency, resiliency, and sustainability of infrastructure and natural systems. His research interests include hydro-informatics, atmospheric-informatics, traffic data, structural health, smart infrastructure systems, and connected transportation.